

Reconfigurable Diodes Based on Vertical WSe₂ Transistors with van der Waals Bonded Contacts

Ahmet Avsar, Kolyo Marinov, Enrique Gonzalez Marin, Giuseppe Iannaccone, Kenji Watanabe, Takashi Taniguchi, Gianluca Fiori, and Andras Kis*

New device concepts can increase the functionality of scaled electronic devices, with reconfigurable diodes allowing the design of more compact logic gates being one of the examples. In recent years, there has been significant interest in creating reconfigurable diodes based on ultrathin transition metal dichalcogenide crystals due to their unique combination of gate-tunable charge carriers, high mobility, and sizeable band gap. Thanks to their large surface areas, these devices are constructed under planar geometry and the device characteristics are controlled by electrostatic gating through rather complex two independent local gates or ionic-liquid gating. In this work, similar reconfigurable diode action is demonstrated in a WSe₂ transistor by only utilizing van der Waals bonded graphene and Co/h-BN contacts. Toward this, first the charge injection efficiencies into WSe₂ by graphene and Co/h-BN contacts are characterized. While Co/h-BN contact results in nearly Schottky-barrier-free charge injection, graphene/WSe₂ interface has an average barrier height of ≈80 meV. By taking the advantage of the electrostatic transparency of graphene and the different work-function values of graphene and Co/h-BN, vertical devices are constructed where different gate-tunable diode actions are demonstrated. This architecture reveals the opportunities for exploring new device concepts.

The fascinating properties of graphene have attracted the attention of the research community working toward developing next-generation electronic devices.^[1] Despite the absence of a natural band gap,^[2] various attempts to obtain high on/off current ratios have been demonstrated by utilizing graphene nanoribbons^[3] or integrating it into barristor device configurations.^[4] The observation of a sizeable electronic band gap


in 2D transition metal dichalcogenides (TMDCs)^[5] has stimulated the electronic device research mostly toward these materials,^[6–8] which have been exploited at first in optoelectronic applications, while relying on lateral device configurations. In these devices, two local gates were utilized to control the polarity in a single 2D TMDC layer,^[9–13] and device concepts such as current rectifying diodes, light-emitting diodes, photodetectors, and photovoltaic devices were demonstrated. Similar rectification actions were also achieved by partially doping the TMDC layer using ionic-liquid gating.^[14] While these device characteristics are important for the prospect of using TMDCs in future optoelectronic applications,^[15,16] the implementation of such complex structures in realistic devices poses significant challenges. Toward this, Chuang et al. demonstrated rectifying behavior in MoS₂-based diodes with asymmetric MoO_x and Ni contacts without any need of a complex fabrication process.^[17] Considering the recent demand for expanding the device and circuit geometries in the third dimension,^[18] utilizing an approach based on the deposition of thick metals could limit further device miniaturization and, more importantly, it could preclude benefiting from various device functionalities such as the gating effect.

In order to achieve high device performance in TMDC-based devices, it is critical to form contacts which exhibit low contact resistance and allow Schottky-barrier-free charge injection. Most of evaporated metals, independently of their work functions, exhibit Fermi level pinning to the conduction band of TMDC layers.^[19,20] Such directly evaporated contact materials on top of 2D materials are bonded by ionic/covalent bonds and induce unavoidable defects which cause significant Schottky barrier heights and high contact resistance.^[19,20] Atomically thin van der Waals contacts could provide a solution to these problems. In the case of MoS₂, graphene was recently utilized as the contact material.^[21,22] These devices exhibited nearly Schottky-barrier-free charge injection and, as a result, very high quality charge transport characteristics were observed. Moreover, the work function of graphene is gate tunable due to its linear dispersion relationship,^[23] and it is almost electrostatically transparent since the screening length exceeds the thickness of the single atomic layer. This makes graphene

Dr. A. Avsar, Dr. K. Marinov, Prof. A. Kis
Electrical Engineering Institute
Institute of Materials Science and Engineering
École Polytechnique Fédérale de Lausanne (EPFL)
Lausanne CH-1015, Switzerland
E-mail: andras.kis@epfl.ch

Dr. E. G. Marin, Prof. G. Iannaccone, Prof. G. Fiori
Dipartimento di Ingegneria dell'Informazione
Università di Pisa
Pisa 56122, Italy

Dr. K. Watanabe, Dr. T. Taniguchi
Advanced Materials Laboratory
National Institute for Materials Science
1-1 Namiki, Tsukuba 305-0044, Japan

 The ORCID identification number(s) for the author(s) of this article can be found under <https://doi.org/10.1002/adma.201707200>.

DOI: 10.1002/adma.201707200

an extremely useful choice as a bottom contact material for gate-tunable vertical transistor devices.^[24] However, considering the different band structures of TMDC crystals, it is not known if graphene could be an ideal contact material for other TMDCs as well. Similar to graphene, Co/h-BN stacks also hold a great promise as a contact material.^[25,26] Besides being utilized as a high-quality spin injector,^[27] they are expected to eliminate Fermi level pinning and hence prevent the formation of metal-induced defects.^[28] Finally, once h-BN is contacted to Co, electrons are accumulated close to Co and depletion of electrons is expected close to h-BN. This forms interface dipoles which push electrons toward Co because of Pauli exchange repulsion and therefore cause a reduction in the work function of Co, from 5.2 to 3.7 eV.^[28] Such a change in the effective work function of contact material would bring the Fermi level to just below the conduction band minimum of a TMDC crystal and therefore allow Schottky-barrier-free charge injection.

In this manuscript, we report a comprehensive study of transport characteristics of thin WSe₂ contacted to graphene and Co/h-BN in various device configurations. WSe₂ is of special interest among 2D semiconducting materials due to the presence of a very high valence band splitting^[29] and high electronic mobility.^[30] WSe₂ has also been considered to be the most suitable candidate for low-power operation at the 2028 International Technology Roadmap for Semiconductors node due to its optimum effective mass for driving the maximum current.^[31] Therefore, we use WSe₂ as the active channel material in our study and contact it from bottom and top sides with graphene and Co/h-BN, respectively (Figure 1a). This geometry not only allows us to directly compare the contact properties of graphene and Co/h-BN to WSe₂ but also to build gate-tunable vertical devices due to different work-function values of van der Waals bonded graphene and Co/h-BN contacts. In this device architecture, we also benefit from the electrostatic transparency of bottom graphene contacts. h-BN in our device can be indeed considered as a transparent contact at this thickness range (three layers) despite its large band gap of ≈6 eV.^[32] Metal contacts (30 nm Co and 5 nm Ti) to graphene and h-BN are formed using electron beam evaporation under high-vacuum conditions. The Ti layer acts as a capping layer to prevent the oxidation of the Co film. Optical and atomic force microscopy images after the metallization process are shown in Figure 1b and Figure 1c, respectively. The details of device fabrication are presented in the “Experimental Section” and Figure S1,

Supplementary Information. Here, we would like to note that we do not expect any shunting effect in lateral transport by the graphene when using the Co/h-BN contacts or through Co/h-BN when using the graphene contacts as a result of our careful device design (Figure S3, Supporting Information). The current (*I*_{SD}) through WSe₂-based devices is characterized as a function of back-gate voltage (*V*_{BG}), drain–source bias (*V*_{SD}), and temperature. Since hysteresis in transport curves is an important parameter to be considered while analyzing results, a great attention is given to this point. We followed the same measurement protocol: *V*_{BG} and *V*_{SD} were swept from negative values (or 0) to positive values under the same ramping rate in order to eliminate the effect of hysteresis (see the Supporting Information).

Prior to any vertical transport characterization, we first measure the charge transport in planar geometry in order to study the properties of graphene contacts. Figure 2a shows the *V*_{BG} dependence of *I*_{SD} at fixed *V*_{SD} values of 0.3 and 1 V where we observe dominant n-type transport behavior with on/off current ratios exceeding 10⁵. As shown in Figure 2b (inset), the *I*_{SD}–*V*_{SD} relation is highly nonlinear, independent of the *V*_{BG} value. This indicates the presence of a Schottky barrier. This is supported by the observation of a strong temperature dependence of *I*_{SD}–*V*_{BG} as shown in Figure 2b. To quantify this, we study the *I*_{SD}–*V*_{SD} relation as a function of *V*_{BG} and temperature (Figure 2b; Figure S5, Supporting Information). Data are analyzed using the thermionic emission model^[33]

$$I_{SD} = AA^*T^{1.5} \exp\left[\frac{-e}{k_B T} \left(\Phi_B - \frac{V_{SD}}{n}\right)\right] \quad (1)$$

where *A* is the contact area, *A** is the 2D Richardson constant, *e* is the electron charge, *k*_B is the Boltzmann constant, Φ_B is the Schottky barrier height, and *n* is the ideality factor. From here, we extract a Schottky barrier height of ≈135 ± 20 meV near the threshold voltage (Figure 2c; Figure S5, Supporting Information). Note that the barrier height strongly depends on *V*_{BG} and is reduced to ≈60 meV as *V*_{BG} increases. This result is rather surprising as graphene contacts have been reported to enable a barrier-free charge injection into MoS₂^[22,34] and black phosphorus (BP)^[35,36]-based transistors, thanks to the relative band alignment of 2D semiconducting crystals/graphene. However, the graphene work function is further away from the conduction band of WSe₂^[37] than of MoS₂ and BP, resulting in a sizable charge injection barrier.

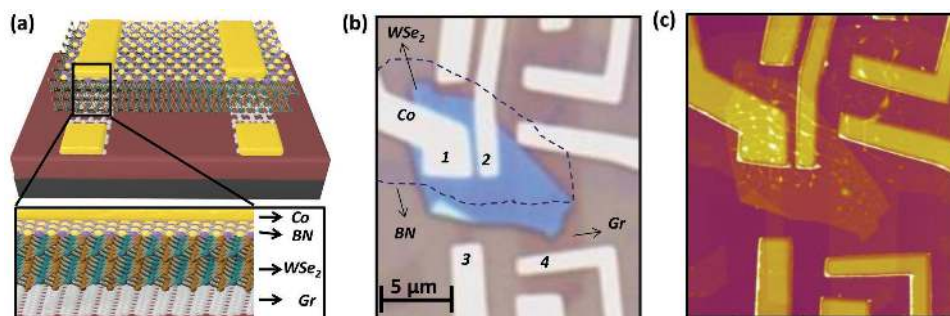


Figure 1. Device structure. a) Schematics of the device. WSe₂ (≈8 nm thick) is bottom contacted with graphene and top contacted with Co/h-BN. b) Optical image of the completed device. Contacts 1 and 2 are Co/h-BN, and contacts 3 and 4 are graphene. The black dotted line outlines the h-BN. c) Atomic force microscopy image of the device shown in panel (b). Height range is 60 nm.

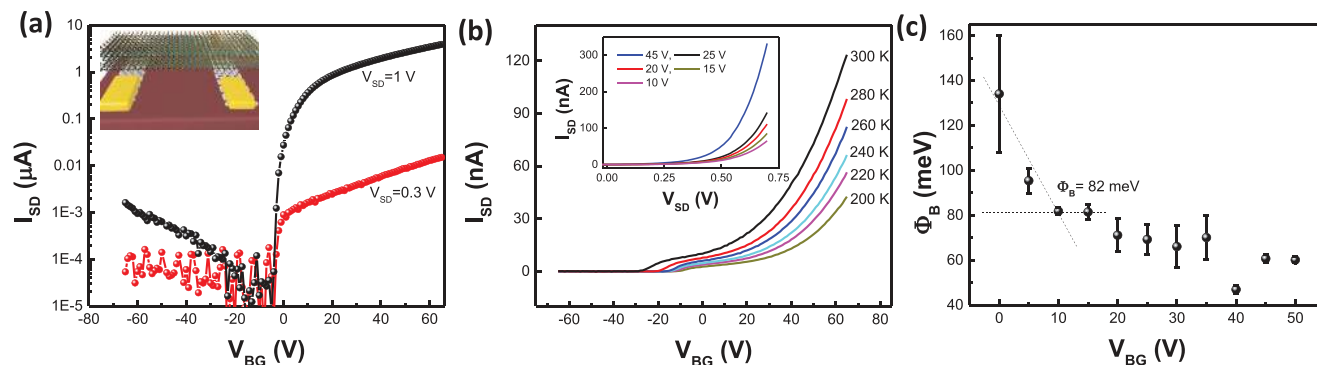


Figure 2. Transport characteristics of graphene-contacted WSe₂. a) Back-gate voltage (V_{BG}) dependence of I_{SD} measured using graphene contacts at room temperature. The inset shows the device schematics. b) V_{BG} dependence of I_{SD} at different temperature values. The inset shows the room-temperature I_{SD} - V_{SD} characteristics at fixed V_{BG} values. c) V_{BG} dependence of the extracted Schottky barrier heights.

Next, we study the properties of Co/h-BN contacts and compare them with graphene contacts. **Figure 3a** shows the V_{BG} dependence of WSe₂ conductivity measured using Co/h-BN and graphene contacts. With Co/h-BN contacts, we also observe n-type transistor behavior in WSe₂ with an on/off current ratio of $\approx 10^5$. To analyze the interface properties of Co/h-BN and WSe₂, we study the I_{SD} - V_{SD} relation which is found to be nearly linear (**Figure 3b**, inset). This indicates the formation of Ohmic contacts and is supported by the observation of an almost temperature-independent I_{SD} - V_{SD} characteristics (**Figure 3b**). Such temperature insensitivity suggests that thermionic emission is not the dominant transport mechanism in these Co/h-BN contacted WSe₂ devices. To confirm this, we analyze the data using the thermionic emission model where we find that the extracted Schottky barrier height values are indeed negative. This confirms that thermionic emission is not relevant in our devices, in good agreement with recent theoretical predictions.^[28]

Next, we study the temperature dependence of I_{SD} - V_{BG} at a fixed V_{SD} value of 0.5 V (**Figure 3c**). From the linear regime of I_{SD} - V_{BG} curves, we estimate the two-terminal (2T) field effect mobility μ by using $\mu = \frac{L}{W} \frac{1}{C_{BG}} \frac{1}{V_{SD}} \frac{dI_{SD}}{dV_{BG}}$ where L and W are the length and width of the measured junction and C_{BG} is the back-gate capacitance. Mobility is nearly temperature independent

between 15 and 75 K and decreases with increasing temperature. The extracted μ at 15 K is $\approx 165 \text{ cm}^2 \text{ V}^{-1} \text{ s}^{-1}$ and decreases to $\approx 110 \text{ cm}^2 \text{ V}^{-1} \text{ s}^{-1}$ at room temperature. This is comparable to values extracted from four-contact measurements on liquid-gated devices.^[38] Here the scaling of $2T \mu$ on temperature is important. Such a temperature dependence of μ has been observed in the four-terminal (4T) configuration with the charge transport in the low-temperature region ($15 \text{ K} < T < 75 \text{ K}$) limited by the impurity scattering whereas phonon scattering becomes dominant at $T > 75 \text{ K}$.^[39] The minimized Schottky barrier allows us to observe such remarkable temperature dependence also in the 2T configuration. Here we also note that the extracted μ values are underestimated as there is a finite contact resistance contribution to the total device resistance.

If we compare the transport characteristics of WSe₂ measured with Co/h-BN and graphene contacts (**Figure 3a**), two distinguishing features stand out from their transport curves. First, the conductivity value measured with graphene contacts is an order of magnitude smaller than the one measured with Co/h-BN. Second, the threshold voltage (V_{TH}) measured with graphene contacts is $\approx 12.2 \text{ V}$ lower than that of Co/h-BN. Both of these observations suggest that the band alignment is different for graphene and Co/h-BN contacts due to their different work-function values. This allows the possibility of achieving different diode characteristics as the gate bias is modulated

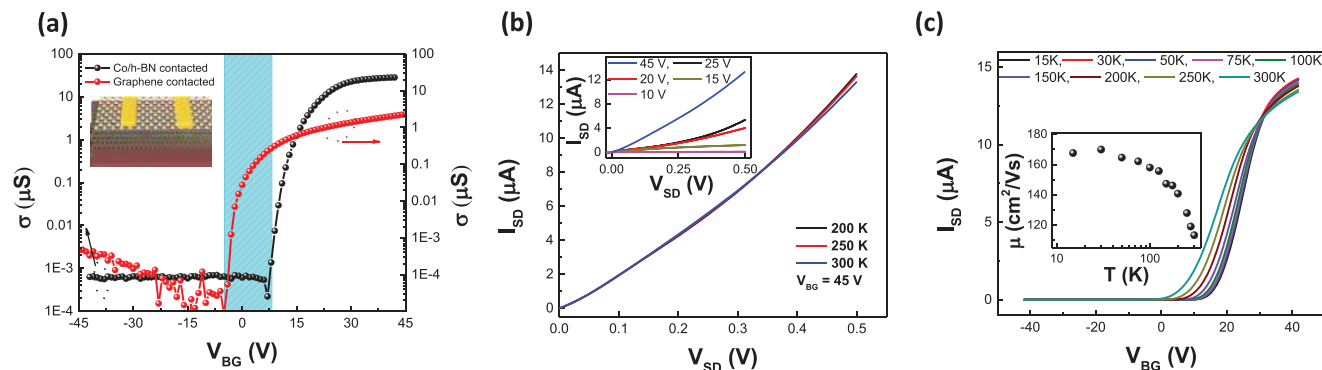


Figure 3. Transport characteristics of Co/h-BN contacted WSe₂. a) V_{BG} dependence of the σ measured with graphene (red line, $V_{SD} = 1 \text{ V}$) and Co/h-BN contacts (black line, $V_{SD} = 0.5 \text{ V}$) at room temperature. The inset shows the device schematics. b) V_{BG} dependence of I_{SD} measured at different temperature values. The inset shows the I_{SD} - V_{SD} characteristics at fixed V_{BG} values. c) V_{BG} dependence of I_{SD} measured in the two-terminal (2T) configuration at different temperature points. The inset shows temperature dependence of 2T mobility.

if source and drain contacts are fabricated using Co/h-BN and graphene, respectively. Such gate-tunable measurements are possible thanks to the electrostatic transparency of bottom graphene contacts due to its thickness being smaller than the screening length.

Toward this, we study the vertical transport by utilizing Co/h-BN and graphene as source and drain electrodes, respectively. Due to the presence of very high “off” current values in the direct vertical device configuration (Figure S6, Supporting Information), we introduce an extra pathway along the planar direction which yields higher on/off current ratios. As the vertical direction exhibits higher conductance, we expect current to flow from the Co/h-BN contact first vertically, then laterally at the bottom part of thin WSe₂, and finally into the graphene layer. The device schematics and optical image of the completed device are shown in Figure 4a (inset). In order to further improve the device quality, here we fabricated a similar Co/h-BN/WSe₂/graphene heterostructure on a h-BN substrate which is back-gated through a graphite contact.

Figure 4a shows the V_{BG} dependence of the I_{SD} at fixed V_{SD} values of 1, 2, and 3 V. Here V_{SD} is applied between the Co/h-BN and graphene electrode (grounded), while V_{BG} is applied through the h-BN substrate. The device shows a dominant n-type behavior but a weak p-type transport characteristic is also observed at negative V_{BG} values. Due to the reduced back-gate dielectric thickness and improved sample/substrate interface, the subthreshold swing (SS) value is enhanced to ≈ 260 mV dec⁻¹. While this SS value is more than an order of magnitude improved compared to the ≈ 270 nm thick SiO₂ substrate case, it could be further improved by decreasing the h-BN thickness. The current on/off ratio in this device is $\approx 10^6$, more than four orders of magnitude higher than compared to the direct tunneling device in the vertical geometry (Figure S6, Supporting Information).

Since the work functions of graphene and h-BN are different, the vertical transport properties of this device should strongly depend on the V_{BG} modulation. In order to demonstrate this, we study the I_{SD} - V_{SD} relation at different V_{BG} values (Figure 4b). At $V_{BG} = 7$ V, where the device is the most conductive, I_{SD} - V_{SD} shows a nonsymmetric relationship. The current under forward bias is several times larger than the current under backward bias due to more efficient Co/h-BN contacts. This is demonstrated by the observation of higher conductivity values measured with Co/h-BN compared to graphene at high V_{BG} values (Figure 3a). As the V_{BG} value is reduced, forward and backward bias currents become comparable. In the very low V_{BG} range

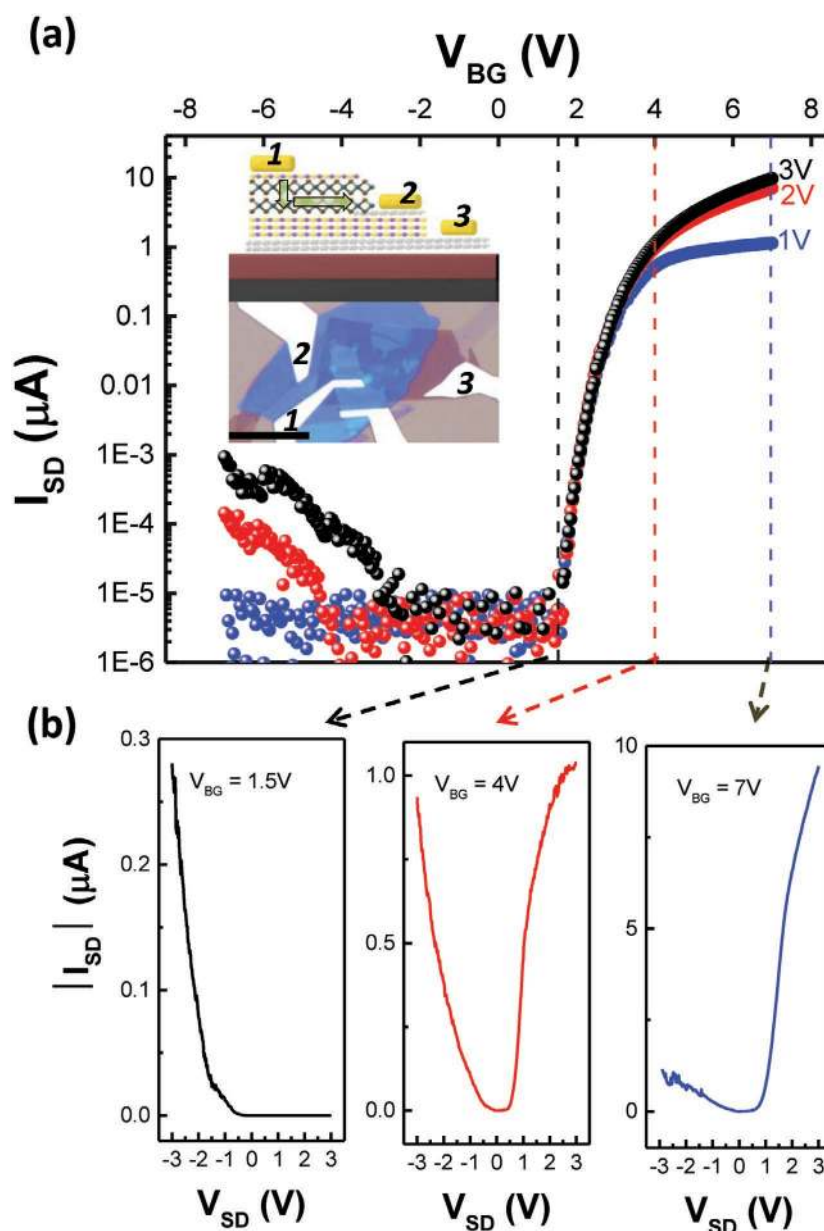


Figure 4. Diagonal transport across graphene and Co/h-BN contacts. a) V_{BG} dependence of I_{SD} at fixed source–drain bias voltage ($V_{SD} = 1, 2,$ and 3 V) at RT. The inset shows the schematics and the optical image of the device. WSe₂ (≈ 8 nm) is contacted from the bottom using graphene (2) and from the top using Co/h-BN (1). h-BN (≈ 25 nm) and a graphite layer (3) are used as a substrate and back-gate contact, respectively. b) V_{SD} dependence of I_{SD} at fixed V_{BG} values.

($2 \text{ V} < V_{BG} < 0 \text{ V}$), the device shows a completely reversed diode behavior (Figure 4b). Here the observed rectification ratio is as high as 10^5 . The reversed diode behavior is caused by the asymmetric contacts, with only the graphene contact being able to drive current at this V_{BG} range which is supported by the observation of a higher V_{TH} value with Co/h-BN contacts.

In the intermediate V_{BG} range, the biasing characteristic (I_{SD} - V_{SD}) shows very distinct features. As shown in Figure 5a, we reach current saturation in the forward bias range. The bias voltage where current saturation is observed decreases as the V_{BG} value is reduced (Figure S7, Supporting

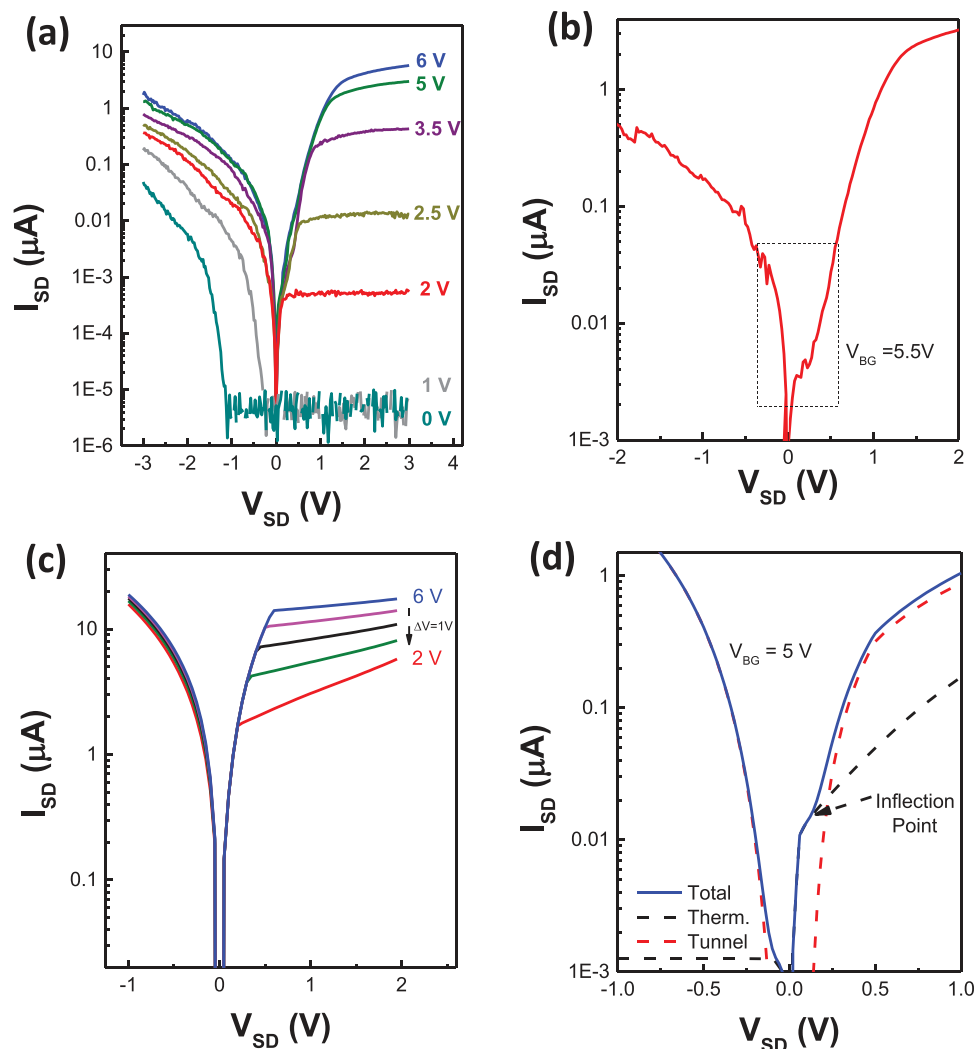


Figure 5. Diagonal transport across graphene and Co/h-BN contacts. a,b) V_{SD} dependence of I_{SD} at fixed V_{BG} values. Numerical model showing c) the source of forward bias saturation and d) asymmetry between backward and forward bias currents at $V_{BG} = 5$ V.

Information). For instance, we observe current saturation at $V_{SD} \approx 0.87$ V for $V_{BG} = 3.5$ V whereas it is observed only at ≈ 0.15 V for $V_{BG} = 2$ V. Note that such current saturation is not observed in the backward bias region. The corresponding simplified band diagrams for both forward and backward bias conditions are shown in Figure S8-9 in the Supporting Information. When a positive V_{SD} value is applied, electrons are injected from the graphene contact into the conduction band of WSe_2 through a thin barrier. They are finally detected using the Co/h-BN contacts via a tunneling process. The width of the barrier saturates as the positive bias is increased. This limits the charge injection at higher V_{SD} values and hence the current saturates. Since the barrier width further increases as the V_{BG} is reduced, we observe the saturation at smaller V_{SD} values. Near $V_{BG} = 5.5$ V, we report a special asymmetry in the $I_{SD}-V_{SD}$ curve where a distortion in the forward bias current regime is observed (highlighted with a dotted box in Figure 5b). At first glance, this looks like the trend toward negative differential resistance effect previously observed for 2D-material-based tunnel field effect transistors.^[40] However, it is impossible to

realize the band-to-band tunneling effect at this gate voltage range in our device since both graphene and Co/h-BN contacts can only inject electrons. Instead, the occurrence of this inflection point in the biasing characteristic could be related to the interplay between tunneling and thermionic charge injection by Co/h-BN and graphene contacts, respectively.

In order to fully understand the origin of the effects occurring at the intermediate V_{BG} range, we have developed a simple analytical model by taking into account both the thermionic and tunneling components of the current. In particular, the thermionic current (i.e., the contribution of carriers flowing over the energy barrier) is modeled through the Richardson's model^[41] considering Fermi-Dirac statistics. The tunneling current (i.e., the contribution of carriers flowing through the energy barrier) is modeled by means of the Wentzel-Kramers-Brillouin approximation.^[42] The carrier total kinetic energy is decomposed into transversal-to-the-barrier and perpendicular-to-the-barrier components, considering a linear dispersion relationship for the transverse modes of graphene close to the Dirac point. The role of the h-BN/graphite back contact is included in

the numerical model by solving the 1D Poisson equation along the WSe₂/h-BN/graphene direction.

As can be seen in Figure 5c,d, despite the simplicity of the model, the results are in good agreement with the experimental ones for $V_{BG} > 3$ V, and, in particular, they reproduce the saturation and the inflection point in forward bias, and their dependence on V_{BG} . For negative V_{SD} , the current is mainly due to tunneling through the small Co/h-BN/WSe₂ barrier. On the contrary, for positive V_{SD} , the barrier width increases and hence the current leads to the saturation of the current at large V_{SD} as shown in Figure S8 in the Supporting Information. In Figure 5d, we show the contribution of tunneling and thermionic components of the current as well as the total current. As can be seen, we manage to capture the asymmetry observed in the experimental data (Figure 5b), showing that the observed current inflection in the forward bias current can be explained by the interplay between thermionic and tunneling currents (Figure S9, Supporting Information).

In conclusion, we have demonstrated an extensive study of transport properties of ultrathin WSe₂ crystals by employing van der Waals bonded Co/h-BN and graphene contacts. Lateral transport measurements reveal that the Co/h-BN contacts are nearly barrier free whereas graphene contacts have an average Schottky barrier height of ≈ 80 meV. Benefiting from the electrostatic transparency of the graphene contacts, we have also characterized its charge transport properties along the vertical direction. Due to different work functions of graphene and Co/h-BN contacts, we observe different I_{SD} - V_{SD} characteristics including a normal diode, reversed diode, and a new diode behavior where the forward bias current is saturated due to interplay between thermionic and tunneling currents, resulting in the realization of a reconfigurable vertical diode. Our results provide important insights for the development of next-generation transistor applications based on 2D materials.

Experimental Section

Material Transfer and Device Fabrication: The device fabrication was started with the micromechanical exfoliation of graphene stripes onto an Si/SiO₂ (≈ 270 nm thick) wafer. WSe₂ was similarly exfoliated onto a separate Si/SiO₂ wafer. WSe₂ was then picked up by melting the polypropylene carbonate (PPC) polymer at an elevated temperature (≈ 85 °C) and its subsequent solidification by natural cooling down. By using a home-made transfer stage, the WSe₂ crystal was deposited onto the previously exfoliated graphene stripes. The PPC layer was later removed using chloroform. This transfer process was repeated for the ≈ 3 layer thick BN crystal. The final heterostructure (graphene/WSe₂/h-BN) was annealed at 250 °C for 6 h under high-vacuum conditions after each transfer process in order to improve bonding between the layers and minimize the amount of transfer-related residues. Electrode masks were prepared using a standard electron beam lithography process, and metals (30 nm Co and 5 nm Ti) were deposited using an electron beam evaporator under high-vacuum conditions. Optical and atomic force microscopy images after the metallization process are shown in Figure 1b and Figure 1c, respectively. Electronic transport measurements were performed as a function of back-gate voltage (V_{BG}), source-drain bias voltage (V_{SD}), and temperature.

Numerical Model: 1D Poisson equation was solved to model the electrostatics of the WSe₂/h-BN/graphene junction. Free charge in correspondence of graphene was computed considering a linear dispersion relation, while a parabolic energy dispersion was taken into account for out-of-plane thermionic current as in ref. [41] with $m^* = 0.5$.

Once the energy potential distribution was obtained, the current was computed using the Richardson's model with Fermi-Dirac statistics for modeling the thermionic current and the Wentzel-Kramers-Brillouin approximation for the tunneling component of the current. In the adopted model, the graphene work function was exploited as a fitting parameter (ranging from 4.0 to 4.6 eV), consistently with experimental results available in the literature.^[43]

Supporting Information

Supporting Information is available from the Wiley Online Library or from the author.

Acknowledgements

A.A., K.M., and A.K. would like to acknowledge support by the European Research Council (ERC, Grant No. 682332), Swiss National Science Foundation (Grant No. 157739), and Marie Curie-Sklodowska COFUND (Grant No. 665667). A.K. and G.F. acknowledge funding from the European Union's Horizon 2020 Research and Innovation programme under grant agreement No. 696656 (Graphene Flagship). K.W. and T.T. acknowledge support from the Elemental Strategy Initiative conducted by the MEXT, Japan, and JSPS KAKENHI (Grant Nos. JP15K21722 and JP25106006).

Conflict of Interest

The authors declare no conflict of interest.

Keywords

2D materials, contact engineering, field effect transistor devices, reconfigurable devices, van der Waals contact

Received: December 11, 2017

Revised: January 20, 2018

Published online:

- [1] F. Schwierz, *Nat. Nanotechnol.* **2010**, *5*, 487.
- [2] A. H. Castro Neto, N. M. R. Peres, K. S. Novoselov, A. K. Geim, *Rev. Mod. Phys.* **2009**, *81*, 109.
- [3] M. Han, B. Özyilmaz, Y. Zhang, P. Kim, *Phys. Rev. Lett.* **2007**, *98*, 206805.
- [4] H. Yang, J. Heo, S. Park, H. J. Song, D. H. Seo, K.-E. Byun, P. Kim, I. Yoo, H.-J. Chung, K. Kim, *Science* **2012**, *336*, 1140.
- [5] K. F. Mak, C. Lee, J. Hone, J. Shan, T. F. Heinz, *Phys. Rev. Lett.* **2010**, *105*, 136805.
- [6] B. Radisavljevic, A. Radenovic, J. Brivio, V. Giacometti, A. Kis, *Nat. Nanotechnol.* **2011**, *6*, 147.
- [7] S. Manzeli, D. Ovchinnikov, D. Pasquier, O. V. Yazyev, A. Kis, *Nat. Rev. Mater.* **2017**, *2*, 17033.
- [8] D. Jariwala, T. J. Marks, M. C. Hersam, *Nat. Mater.* **2016**, *16*, 170.
- [9] B. W. H. Baugher, H. O. H. Churchill, Y. Yang, P. Jarillo-Herrero, *Nat. Nanotechnol.* **2014**, *9*, 262.
- [10] A. Pospischil, M. M. Furchi, T. Mueller, *Nat. Nanotechnol.* **2014**, *9*, 257.
- [11] J. S. Ross, P. Klement, A. M. Jones, N. J. Ghimire, J. Yan, D. G. Mandrus, T. Taniguchi, K. Watanabe, K. Kitamura, W. Yao, D. H. Cobden, X. Xu, *Nat. Nanotechnol.* **2014**, *9*, 268.

- [12] G. V. Resta, S. Sutar, Y. Balaji, D. Lin, P. Raghavan, I. Radu, F. Catthoor, A. Thean, P.-E. Gaillardon, G. de Micheli, *Sci. Rep.* **2016**, *6*, 29448.
- [13] S. Sutar, P. Agnihotri, E. Comfort, T. Taniguchi, K. Watanabe, J. U. Lee, *Appl. Phys. Lett.* **2014**, *104*, 122104.
- [14] S. Y. Lee, U. J. Kim, J. Chung, H. Nam, H. Y. Jeong, G. H. Han, H. Kim, H. M. Oh, H. Lee, H. Kim, Y.-G. Roh, J. Kim, S. W. Hwang, Y. Park, Y. H. Lee, *ACS Nano* **2016**, *10*, 6100.
- [15] O. Lopez-Sanchez, D. Lembke, M. Kayci, A. Radenovic, A. Kis, *Nat. Nanotechnol.* **2013**, *8*, 497.
- [16] F. H. L. Koppens, T. Mueller, P. Avouris, A. C. Ferrari, M. S. Vitiello, M. Polini, *Nat. Nanotechnol.* **2014**, *9*, 780.
- [17] S. Chuang, C. Battaglia, A. Azcatl, S. McDonnell, J. S. Kang, X. Yin, M. Tosun, R. Kapadia, H. Fang, R. M. Wallace, A. Javey, *Nano Lett.* **2014**, *14*, 1337.
- [18] M. M. Shulaker, G. Hills, R. S. Park, R. T. Howe, K. Saraswat, H.-S. P. Wong, S. Mitra, *Nature* **2017**, *547*, 74.
- [19] C. Kim, I. Moon, D. Lee, M. S. Choi, F. Ahmed, S. Nam, Y. Cho, H.-J. Shin, S. Park, W. J. Yoo, *ACS Nano* **2017**, *11*, 1588.
- [20] Y. Guo, D. Liu, J. Robertson, *Appl. Phys. Lett.* **2015**, *106*, 173106.
- [21] X. Cui, G.-H. Lee, Y. D. Kim, G. Arefe, P. Y. Huang, C.-H. Lee, D. A. Chenet, X. Zhang, L. Wang, F. Ye, F. Pizzocchero, B. S. Jessen, K. Watanabe, T. Taniguchi, D. A. Muller, T. Low, P. Kim, J. Hone, *Nat. Nanotechnol.* **2015**, *10*, 534.
- [22] Y. Liu, H. Wu, H.-C. Cheng, S. Yang, E. Zhu, Q. He, M. Ding, D. Li, J. Guo, N. O. Weiss, Y. Huang, X. Duan, *Nano Lett.* **2015**, *15*, 3030.
- [23] Y.-J. Yu, Y. Zhao, S. Ryu, L. E. Brus, K. S. Kim, P. Kim, *Nano Lett.* **2009**, *9*, 3430.
- [24] T. Georgiou, R. Jalil, B. D. Belle, L. Britnell, R. V. Gorbachev, S. V. Morozov, Y.-J. Kim, A. Gholinia, S. J. Haigh, O. Makarovskiy, L. Eaves, L. A. Ponomarenko, A. K. Geim, K. S. Novoselov, A. Mishchenko, *Nat. Nanotechnol.* **2013**, *8*, 100.
- [25] A. Avsar, J. Y. Tan, X. Luo, K. H. Khoo, Y. Yeo, K. Watanabe, T. Taniguchi, S. Y. Quek, O. Barbaros, *Nano Lett.* **2017**, *17*, 5361.
- [26] X. Cui, E.-M. Shih, L. A. Jauregui, S. H. Chae, Y. D. Kim, B. Li, D. Seo, K. Pistunova, J. Yin, J.-H. Park, H.-J. Choi, Y. H. Lee, K. Watanabe, T. Taniguchi, P. Kim, C. R. Dean, J. C. Hone, *Nano Lett.* **2017**, *17*, 4781.
- [27] A. Avsar, J. Y. Tan, M. Kurpas, M. Gmitra, K. Watanabe, T. Taniguchi, J. Fabian, B. Özyilmaz, *Nat. Phys.* **2017**, *13*, 888.
- [28] M. Farmanbar, G. Brocks, *Phys. Rev. B* **2015**, *91*, 161304.
- [29] K. F. Mak, K. He, J. Shan, T. F. Heinz, *Nat. Nanotechnol.* **2012**, *7*, 494.
- [30] B. Fallahzad, H. C. P. Movva, K. Kim, S. Larentis, T. Taniguchi, K. Watanabe, S. K. Banerjee, E. Tutuc, *Phys. Rev. Lett.* **2016**, *116*, 86601.
- [31] S. S. Sylvia, K. Alam, R. K. Lake, *IEEE J. Explor. Solid-State Comput. Devices Circuits* **2016**, *2*, 28.
- [32] K. Watanabe, T. Taniguchi, H. Kanda, *Nat. Mater.* **2004**, *3*, 404.
- [33] J.-R. Chen, P. M. Odenthal, A. G. Swartz, G. C. Floyd, H. Wen, K. Y. Luo, R. K. Kawakami, *Nano Lett.* **2013**, *13*, 3106.
- [34] Y. Choi, J. Kang, D. Jariwala, M. S. Kang, T. J. Marks, M. C. Hersam, J. H. Cho, *Adv. Mater.* **2016**, *28*, 3742.
- [35] A. Avsar, I. J. Vera-Marun, J. Y. Tan, K. Watanabe, T. Taniguchi, A. H. Castro Neto, B. Özyilmaz, *ACS Nano* **2015**, *9*, 4138.
- [36] J. Kang, D. Jariwala, C. R. Ryder, S. A. Wells, Y. Choi, E. Hwang, J. H. Cho, T. J. Marks, M. C. Hersam, *Nano Lett.* **2016**, *16*, 2580.
- [37] C. Gong, H. Zhang, W. Wang, L. Colombo, R. M. Wallace, K. Cho, *Appl. Phys. Lett.* **2013**, *103*, 53513.
- [38] A. Allain, J. Kang, K. Banerjee, A. Kis, *Nat. Mater.* **2015**, *14*, 1195.
- [39] B. Radisavljevic, A. Kis, *Nat. Mater.* **2013**, *12*, 815.
- [40] D. Sarkar, X. Xie, W. Liu, W. Cao, J. Kang, Y. Gong, S. Kraemer, P. M. Ajayan, K. Banerjee, *Nature* **2015**, *526*, 91.
- [41] S.-J. Liang, L. K. Ang, *Phys. Rev. Appl.* **2015**, *3*, 14002.
- [42] S. M. Sze, K. K. Ng, *Physics of Semiconductor Devices*, 3rd ed., Wiley, New York, NY **2007**.
- [43] S. S. Datta, D. R. Strachan, E. J. Mele, A. T. C. Johnson, *Nano Lett.* **2009**, *9*, 7.